FIRST-PRINCIPLE ANALYSIS FOR ELECTROMAGNETIC EIGEN MODES IN AN OPTICAL METAMATERIAL SLAB

M. Iwanaga[1, 2, *]

[1]National Institute for Materials Science, 1-1 Namiki, Tsukuba 305-0044, Japan

[2]Japan Science and Technology Agency (JST), PRESTO, 4-1-8 Honcho, Kawaguchi 332-0012, Japan

Abstract—Electromagnetic (EM) eigen modes in a fishnet metamaterial (MM) slab have been comprehensively analyzed in an experimental configuration, based only on precise solutions of Maxwell equations. The EM eigen modes were directly detected from light-absorption peaks. Each mode was explicitly characterized by the dispersion diagram and EM field distributions. It was consequently found that the modes were classified into either inner modes inside the slab or a mode at the interface with the surrounding media. The symmetric properties of the inner modes were clarified using group theory. The interface mode was found to come from surface plasmon polariton at flat metal/insulator interface. The present analysis procedure is generally applicable to MM slabs and enables to clarify the properties without models or assumptions, which have been usually used in MM studies.

1. INTRODUCTION

Metamaterials (MMs) are forming an emerging subfield in artificial electromagnetic (EM) crystals [1–4]. There are definite features in MMs: (i) MMs cover a wide range from acoustic frequencies (kHz) [5–7] to optical frequencies (PHz) [3, 4]; (ii) Most of MMs are composed of metallic artificial structures; (iii) MMs have subwavelength unit cells. The last feature can be regarded as the practical definition.

   In view of EM studies, optical MMs are tough objects to analyze rigorously, partially because metals at optical frequencies have non-negligible loss, i.e., the permittivity ε is complex, so that numerical

* Corresponding author: Masanobu Iwanaga (iwanaga.masanobu@nims.go.jp).

convergence becomes far slow in numerical implementations. In addition, all the optical MMs in experiment were slab structures including stacked layers; therefore, all the modes are leaky from the slab, and the resonant energies are difficult to determine from optical spectra such as reflection and transmission. Actually, in spite of many trials, theoretical methods to solve the resonant modes in MM slabs (for example, Green function method, local-density-of-states theory) have not been established to our knowledge.

Many experimental results on optical MM slabs have been reported so far (e.g., references in [3, 4]). The results were usually interpreted by using effective permittivity-permeability (ε, μ) framework [8], which assumed the validity of EM-field homogenization. However, optical MMs usually have a periodicity of about 1/3 incident wavelength and induce very inhomogeneous EM field distributions on resonances. It has been recently pointed out that, starting from the fundamental Hamiltonian of EM fields and matter, such homogenization is hard to be justified in the standard electromagnetism [9]. Here we show a theoretical analysis based only on EM first-principle computations for a fishnet MM as a representative optical MM. This analysis is expected to directly account for the results in optical measurement and to provide definite insights for the fishnet MM, since recent numerical studies on the plasmonic crystals of complex structures successfully clarified the resonant modes [10–12].

Figure 1 schematically depicts the fishnet MM, which is in a free-standing perforated metal-insulator-metal (MIM) structure in air. Air holes periodically perforate the stacked MIM layers, forming a square array which is assumed to infinitely spread two-dimensionally. The periodicity a was set to be $a = 830\,\text{nm}$ and the diameter of the air holes was set to be $400\,\text{nm}$. Specifically, M was Au and I was Al_2O_3. The thicknesses of the M and I layers were set at 30 and $60\,\text{nm}$, respectively. These structural parameters were taken from an experimental specimen [13].

Fishnet MMs were most extensively studied in experiment [13–21]. Effective negative refractive index was extracted from the fishnet MMs. Several theoretical explanations were proposed so far: some of the theories tried to attribute the electric- and magnetic-field responses to effective ε and μ, respectively [22–24], and others were restricted only to the normal incidence [25, 26]. Thus, the entire view of the EM resonant modes has not been resolved so far. It was shortly shown that the lowest EM mode, thought to be related to the effective negative refractive index, is a peculiar planar mode from the Poynting flux [27]. Thus, the whole view of the EM eigen modes in the fishnet MM has
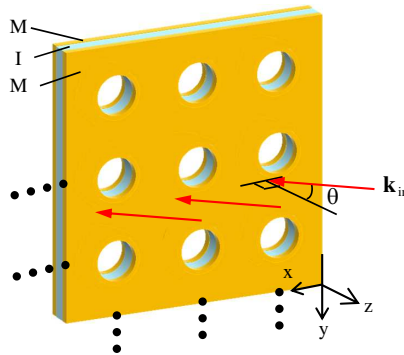
Figure 1. Schematic drawing of a free-standing fishnet MM in air. Coordinate axes and incident wavevector $\mathbf{k}_{in}$ are also shown. The plane of incidence is set to be parallel to the xz plane.

not been clarified to date.

Figure 1 also shows an experimental configuration. An incident plane wave with incident angle θ sheds on the fishnet MM, with incident wavevector $\mathbf{k}_{in}$ in the xz plane. In this configuration, in-plane wavenumber $k_{||}$ is the projection of $\mathbf{k}_{in}$ onto the x axis, defined by $k_{||} = |\mathbf{k}_{in}| \sin \theta$. When incident electric field $\mathbf{E}_{in}$ is parallel to the xz plane, the polarization excites transverse magnetic (TM) modes in the fishnet MM. When the $\mathbf{E}_{in}$ is parallel to the y axis, the polarization induces transverse electric (TE) modes.

In this paper, we clarify the EM eigen modes in a typical MM by numerically resolving Maxwell equations precisely. On the basis of light absorption in the optical configuration, the dispersion diagrams of EM eigen modes are shown in Section 2. From the EM-field distributions in each mode, the EM eigen modes are well characterized in Section 3. This thorough analysis, to our best knowledge, has not been conducted for any MM slab.

2. ABSORPTION SPECTRA AND DISPERSION

2.1. Linear Optical Responses and Absorption

Linear optical responses such as reflectance (R) and transmittance (T) from periodic structures can be computed by solving Fourier-transformed Maxwell equations. The fast convergent algorithms were found in 1990s, so-called the improved Fourier modal method [28] combined with scattering matrix method [29]. In this study, both TE and TM modes were computed, changing incident angle θ from $0°$ to $85°$ at $5°$ steps. The numerical fluctuations of R and T were

estimated to be within 1%. The permittivity of Au was taken from the literature [30]. The permittivities of air and Al_2O_3 were set to be 1.00054 and 2.7225, respectively.

Figure 2(a) shows typical light absorption (A) spectra of the fishnet MM shown in Figure 1. In Figure 2(a), the incident plane wave was TM polarization and the incident angles were 0° (solid line), 10° (blue dashed line), and 20° (dotted line). The absorption A in % was evaluated by subtracting outgoing EM power (the sum of R_{mn} and T_{mn}) from normalized incident EM power (100%):

$$A = 100 - \sum_{m,n}(R_{mn} + T_{mn}) \tag{1}$$

where R_{mn} and T_{mn} are usual notations in diffraction theory, and mn-th reflectance and transmittance, respectively. In particular, R_{00} and T_{00} are R and T, respectively.

Prominent A peaks were observed, explicitly indicating resonant energies of the EM eigen modes in the fishnet MM. This is one of the advantages to examine the A spectra because resonant energies in photonic crystal slabs generally require much elaborate theoretical analysis for optical spectra [31]. The values of A in Figure 2(a) are not large, 20% at most, suggesting that large R appears and that the surface impedance matching is not good. Note that diffraction does not appear under the conditions in Figure 2(a), that is, $R_{mn} = T_{mn} = 0$ for $m \neq 0$ or $n \neq 0$.
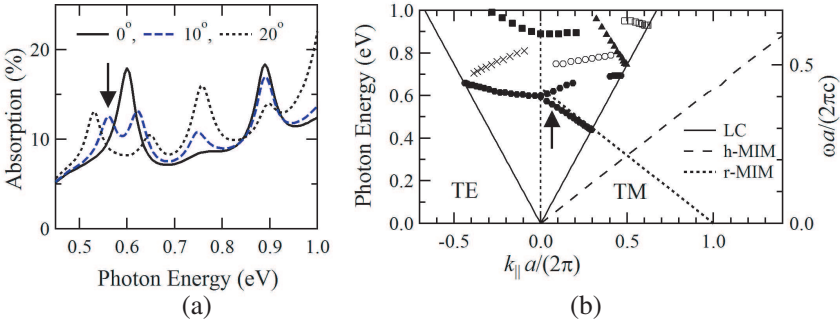

Figure 2. (a) Typical A spectra under TM polarization of the fishnet MM shown in Figure 1. The A spectra are shown at incident angles of $\theta = 0°$ (solid line), 10° (blue dashed line), and 20° (dotted line). (b) Dispersion diagrams of the EM eigen modes, obtained from the A peaks. Solid lines denote the light cone (LC) in air. The dispersion of a homogeneous MIM (h-MIM) waveguide is shown by a dashed line, for comparison. The dotted line represents the dispersion of reduced MIM (r-MIM) mode into the first Brillouin zone.

2.2. Dispersion Analysis

Figure 2(b) shows dispersion diagrams of the EM eigen modes under TM (right) and TE (left) polarizations; the modes in the A peaks are plotted in the plane of normalized in-plane wavenumber $k_{||}a/(2\pi)$ and photon energy in eV. For comparison, the normalized frequency $\omega a/(2\pi c)$ (ω: angular frequency of light, c: the velocity of light in vacuum) is shown on the right axis. Solid oblique lines denote the light cone in air. Here, we consider the situation that plane waves probe the fishnet MM slab, so that all the modes appear above the light cone.

The lowest mode appears at $0.6\,\text{eV}$ and $k_{||} = 0$ in Figure 2(b) and is plotted with closed circles. The lowest mode splits into lower and upper branches at $k_{||} \neq 0$ under TM polarization. The lower branch was well reproduced by a reduced MIM (r-MIM) waveguide mode (dotted line). The details are described later.

The upper branch of the lowest TM mode is not clearly observed at $0.2 < k_{||}a/(2\pi) < 0.4$. This is a finding obtained from computational results and is understood as follows. As is shown in Figure 2(a), the absorption peaks of the upper branch become faint as the incident angle (or $k_{||}$) increases. This is probably because the upper branch gets closer to the nearest-neighbor higher mode, which is called the second TM mode (open circles), and loses the oscillator strength; in fact, it is verified in Figure 2(a) that the absorption peak of the second mode at $0.76\,\text{eV}$ and $\theta = 20°$ is more prominent than the peak of the upper branch at $0.65\,\text{eV}$. Another branch (closed circles) appearing at $k_{||}a/(2\pi) > 0.4$ and $0.7\,\text{eV}$ is possibly connected to the upper branch of the lowest TM mode, because of the similar dispersive behaviors; the reappearance is presumably related to the disappearance of the second mode in Figure 2(b). On the other hand, the upper branch and the TM mode shown by closed triangles have different origins, and consequently it is inferred that they do not take away the oscillator strengths with each other.

In contrast, in Figure 2(b), a single branch of the lowest TE mode appears, which increases in a quadratic manner, suggesting that the lowest mode has two-dimensional (2D) property. The symmetry and dimensionality are examined from the EM field distribution in Subsection 3.1.

Figure 2(b) also shows the second and third (closed squares) TM modes. These lower TM modes are single branch and do not show splitting at all; this is a distinct difference from the lowest TM mode. In addition, the second TM mode is not excited at $k_{||} = 0$, that is, normal incidence. This property suggests that the second mode is forbidden at $k_{||} = 0$; we examine it from the EM field distributions in

Subsection 3.1. From the gradients of dispersions, the group velocities of the second and third TM modes are estimated to be $0.08c$ and $0.002c$, respectively. These modes are thus quite slow; as for the third mode, it behaves like a local mode rather than a propagating mode. Under TE polarization, the second (crosses) and third (closed squares) modes were observed. Obviously, the third TE mode has a common origin with the third TM mode.

The reduced surface-plasmon-polariton (SPP) mode is shown by closed triangles in Figure 2(b). In the present configuration that the fishnet MM stands alone, the background of semi-infinitely thick homogeneous layer is air only. As a result, the reduced SPP has a single branch. The dispersion is reproduced by the dispersion equation for reduced SPP mode, which was already reported [27]. If a substrate such as quartz exists, the second and third modes under TM and TE polarizations are swept away and cannot be observed [27].

There is still another TM mode, which is shown by open squares in Figure 2(b). The mode, which we simply call the fourth TM mode, exists above the reduced SPP mode and is induced simultaneously with diffraction. Thus, the mode is not simply described as a mode of single origin; this is a difference of the fourth mode from the lowest, second, and third modes induced in the subwavelength range.

Let us analyze MIM-inner modes coming from homogeneous (or non-perforated) MIM waveguide modes. Basic properties of homogeneous MIM waveguides were reported in the 1960s [32, 33] and are now well understood; a new twist is to introduce the perforation. To derive the dispersion equation for homogeneous MIM waveguides, it is only necessary to take account of the ordinary boundary conditions assigned to the EM fields in Maxwell equations. In the past reports [32, 33], simplified equations were shown by assuming that all the insulators are vacuum or air. To analyze the present situation, the full dispersion equation is explicitly written as Eq. (A3) in Appendix A. Eq. (A3) cannot be solved analytically; instead, the solutions were found numerically. The lowest one was plotted with dashed line in Figure 2(b).

The periodic structure enables folding of the waveguide mode in the homogeneous MIM structure into the first Brillouin zone. The reduced branch (the dotted line) in Figure 2(b) well reproduces the lower branch of the lowest TM mode. This analysis strongly suggests that the lowest mode originates from the MIM waveguide mode. In addition, the lower branch satisfies the relation of $\partial \omega / (\partial k_{||}) < 0$, suggesting that in-plane negative group velocity is realized; the feature is tested in Figure 3.

Except for the lowest TM mode, other modes in Figure 2(b) cannot

be described simply as reduced MIM waveguide modes. The dispersion in the homogeneous MIM structure is almost linear in the energy range of present interest and cannot reproduce other TM modes by any possible folding into the first Brillouin zone. Even for the second and third TM modes, since the simple analysis is invalid in the free-standing fishnet MM slab, further explorations are carried out through EM-field examinations.

3. EM FIELD DISTRIBUTIONS

3.1. Fishnet MM: Perforated MIM Structure

Figure 3 shows the time-averaged EM power flow, which is equivalent to Poynting flux, at the lower branch of the lowest TM mode. Incident photon energy is $0.560\,\mathrm{eV}$ and incident angle is $10°$ $[k_{||}a/(2\pi) = 0.065]$; the excitation condition is indicated by arrows in Figure 2. The
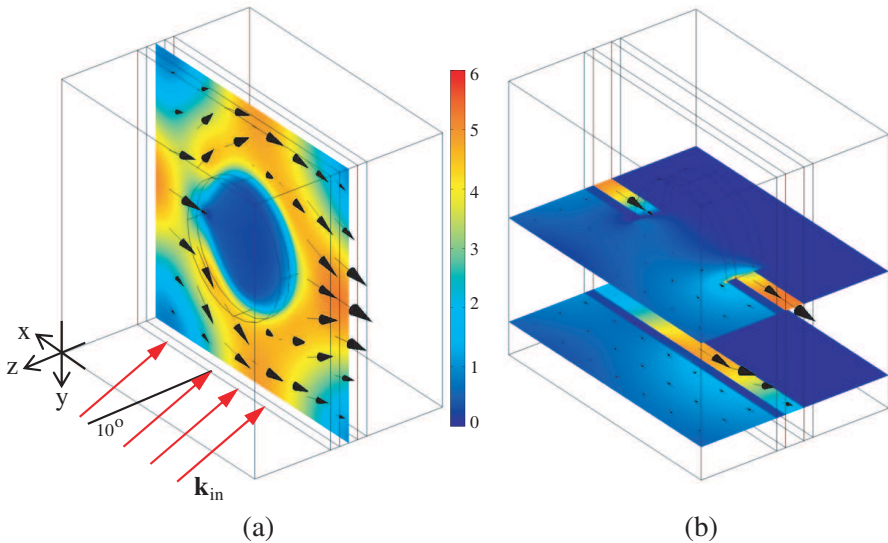

(a)   (b)

Figure 3. Time-averaged EM power flow of the lower branch of the lowest mode under TM polarization. The excitation condition is indicated by arrows in Figure 2. (a) Power flow on a xy section located at the center of the perforated I layer. Incident wavevector $\mathbf{k}_{\mathrm{in}}$ is shown by red arrows. (b) Power flow on the xz sections. The scale bars are in units of $\mathrm{W/m^2}$; the incident power was $1.45\,\mathrm{W/m^2}$ at the xy input port. Black arrows on the sections denote the 3D vectors at each point.

color plots indicate the absolute value of the power flow in units of W/m^2. The input power was set to be $1\,pW$ at the xy input port; accordingly, the input power was $1.45\,W/m^2$. The arrows denote the three-dimensional (3D) vector flows at each point. The left panel shows the power flow on the xy section at the center of the perforated I layer. Incident wavevector $\mathbf{k}_{in}$ is drawn by red arrows. It is clear that the in-plane power flow is negative for the incident x-component. The right panels moreover show that the lowest mode is strongly confined in the I layer of MIM structure; thus, the lowest mode is an MIM-inner mode. We mention that the arrows in the transmitted layer are seemingly missing; actually, they are not omitted but are quite small in comparing to the MIM-inner mode and the power flow in the incident layer, due to low transmittance of about 1%. It was confirmed that the direction of the arrows in the transmitted layer is consistent with that of incidence.

Numerical details of EM field distributions are briefly described as follows. Figure 3 shows the unit domain. Periodic boundary conditions were assigned to the xz and yz boundaries. An incident plane wave travels along the $-z$ direction and comes through the xy input port. In the setting, EM fields were computed by the finite element method (COMSOL Multiphysics). The metallic domains were divided by triangles and tetrahedra with sides of less than $3\,nm$. The insulator and air domains were divided coarsely in comparison with the metals. Numerical tolerance in the computations was suppressed to a few percent. The permittivity of metal (Au) was taken from the literature [30]. As for the input power, here we concentrate on linear optical responses and assume weak excitation. As the input power was $1.45\,W/m^2$, the corresponding electric (E) field in air was $33.1\,V/m$, and the magnetic (H) field was $8.78 \times 10^{-2}\,A/m$. These values are useful for testing resonant enhancements. The following EM field distributions are evaluated similarly.

We here examine the EM eigen modes systematically. Figure 4 shows time-averaged EM power flow (left column: (a), (c), (e)) and snapshots of H field distributions (right column: (b), (d), (f)). Figures 4(a) and 4(b) present the lowest TM mode; Figures 4(c) and 4(d) the second TM mode; Figures 4(e) and 4(g) the third TM mode. The lowest and third modes were excited at the normal incidence ($\theta = 0$, that is, $k_{||} = 0$); the excitation photon energies were 0.600 and 0.895 eV, respectively. Evidently, the net in-plane power flows are zero in Figures 4(a) and 4(e) because of the cancellation of the x and y components. The second TM modes can be excited only at oblique incidence; the incident angle θ was set to be $30°$ $[k_{||}a/(2\pi) = 0.258]$ and the energy was 0.775 eV. The power flow exhibits net x-positive
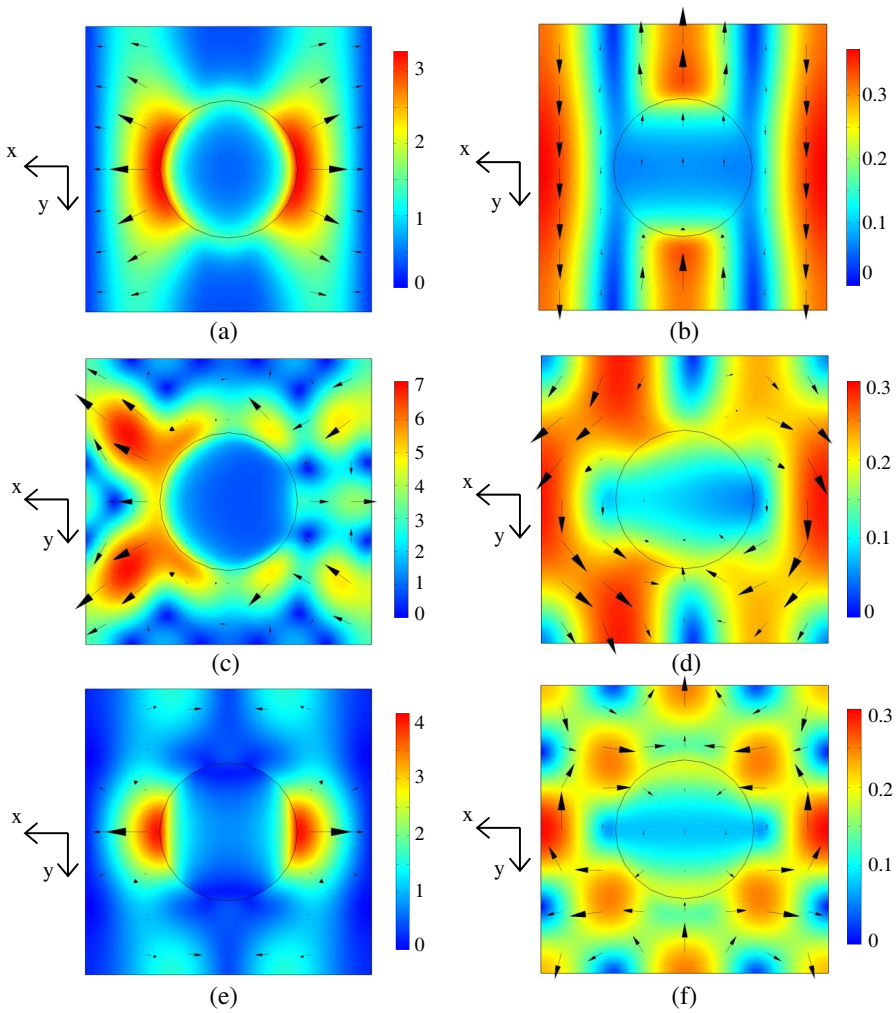
Figure 4. Time-averaged EM power flows and snapshots of H-field distributions under TM polarization. The section was taken at the center of the perforated I layer, similarly to Figure 3(a). The left column shows the EM power flow and the right column displays H field distributions. (a) and (b) are the lowest mode; $\theta = 0°$ ($k_{||} = 0$) and 0.600 eV. (c) and (d) are the second mode; $\theta = 30°$ [$k_{||}a/(2\pi) = 0.258$] and 0.775 eV. (d) and (e) are the third mode; $\theta = 0°$ ($k_{||} = 0$) and 0.895 eV. The scale bars are described in the text.

in-plane power flow. The three modes are enhanced in the perforated I layer, indicating that they are MIM-inner modes. The symmetric properties of the in-plane TM modes are explored in the H field distributions.

In the snapshots of the H field distributions in Figure 4, the phase ϕ of the incident plane wave was determined by setting $\phi = 0$ for $H_y(\phi) = -\cos(\phi)$ at the y edge taking the smallest x value in the xy input port. Figures 4(b) and 4(f) present the H field distributions at the normal incidence, and Figure 4(d) shows the H field distribution at the oblique incidence. The color plots show $|\mathbf{H}|$ distributions and the arrows denote 3D H-field vectors.

The lowest TM mode in Figure 4(b) has simple and symmetric H field distributions. More specifically, the following two properties hold: (i) When 180° rotation around the center of the air hole is conducted, the H field distribution is transformed as $\mathbf{H} \rightarrow -\mathbf{H}$, that is, the intensity is invariant while the vectors have a minus sign; (ii) When incident polarization is changed from the current x polarization to the y polarization, the same mode is induced. These two properties come from the fact that, in terms of group theory, the lowest mode has $\mathcal{E}$ symmetry, which is invariant under C_2 operation (or 180° rotation) except for the sign and is twofold degenerated [34]. The $\mathcal{E}$ symmetric modes are peculiar to 2D periodic systems and cannot be realized in one-dimensional periodic systems. It thus turns out that the lowest mode is a 2D mode.

The second TM mode is an asymmetric mode. It is confirmed as follows. In Figure 4(d), one can infer that it would become symmetric for the air hole as $\theta \rightarrow 0°$ and would finally take $\mathcal{E}$-symmetric distribution at the normal incidence, similarly to the lowest mode. However, the in-plane H fields are dominantly composed of $-y$ components. This means that the in-plane EM power flow is one-directional and cannot be net zero; therefore, asymmetric power flow for the x axis would be induced even at the normal incidence. Of course, the asymmetry is not allowed, which is why the second mode is not excited at normal incidence.

As for the third TM mode, the H field distributions are more complicated, implying that the mode is a higher mode. We again consider the H field distribution in terms of group theory and can identify the third mode $\mathcal{E}$ symmetry. Note that the H field distribution is not closed for 90° rotation and the intensity $|\mathbf{H}|$ is invariant only under C_2 operation.

Figure 5(a) presents R and T spectra under TM polarization at $\theta = 30°$. The shallow R dips at 0.51 and 0.77 eV correspond to the lowest and third TM modes examined so far. The reduced SPP appears

as the deepest R dip and the highest T peak at $0.96\,\mathrm{eV}$. Figures 5(b) and 5(c) show snapshots of E and H field distributions of the reduced SPP, respectively. The phase ϕ was defined similarly to Figure 4. The E field distributions are shown on the xz sections transverse at the center of the air hole and near the bottom of the unit domain. The H field distribution is shown on the yz section transverse at the center of the air hole. The reduced SPP was excited at $k_{\parallel}a/(2\pi) = 0.322$. The field distribution peculiar to the reduced SPP is observed in the H field distributions as shown in Figure 5(c). The H fields are more than 3-fold enhanced near the edge of the air hole in comparison with incident H field. On the other hand, the E fields do not exhibit prominent enhancement except for the edge of the air hole, which implies that the E field is not enhanced by the periodic structure but enhanced locally by the metallic nano-edge.
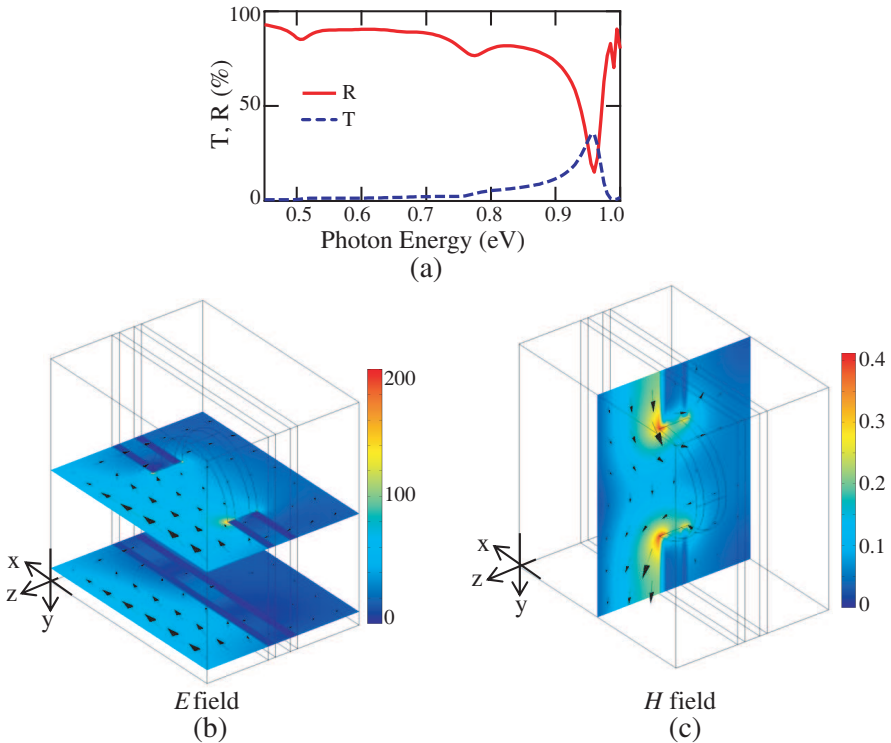

Figure 5. (a) R (red solid line) and T (blue dashed line) spectra under TM polarization at $\theta = 30°$. (b) E field distribution at reduced SPP resonance: $\theta = 30°$ $[k_{\parallel}a/(2\pi) = 0.322]$ and $0.960\,\mathrm{eV}$. (c) H field distribution, corresponding to (b).

The H fields are enhanced by about 5-fold at the lower TM modes (see Figure 4) and at the reduced SPP mode (see Figure 5(c)). Note that the H fields are magnified on resonances irrespective of the MIM-inner modes and the reduced SPP mode. Similar resonant enhancements were found in the E fields.

3.2. Fishnet MM: Perforated MIMIM Structure

Figure 6 shows time-averaged EM power flow in a fishnet MM slab, composed of three M layers and two I layers. The two xy sections were taken at the centers of the I layers. Structural parameters such as the periodicity, the diameter of air holes, and the thickness of the layers were set to be the same as those of the fishnet MM in Subsection 3.1. The lower branch of the lowest TM mode was excited. Incident photon energy was $0.550\,\mathrm{eV}$ and incident angle θ was $30°$ $[k_{||}a/(2\pi) = 0.184]$. This situation is similar to that in Figure 3; the difference is the number of stacked layers. In-plane negative power flows were clearly observed in the two I layers. Concerning the lowest TM mode, the dispersion diagram is similar to the diagram in Figure 2(b). Therefore, similar assignment to the lowest TM mode is valid for the two-I-layers fishnet MM.
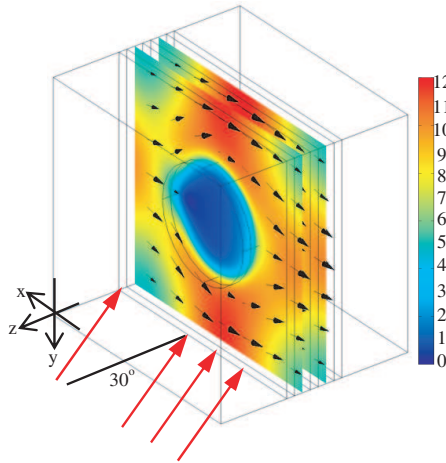

Figure 6. Time-averaged EM power flow in a perforated MIMIM structure. The two xy sections are taken at the centers of the I layers. The lower branch of the lowest mode is excited under TM polarization at $\theta = 30°$ $[k_{||}a/(2\pi) = 0.184]$ and $0.550\,\mathrm{eV}$. The two xy sections are taken at the centers of the I layers.
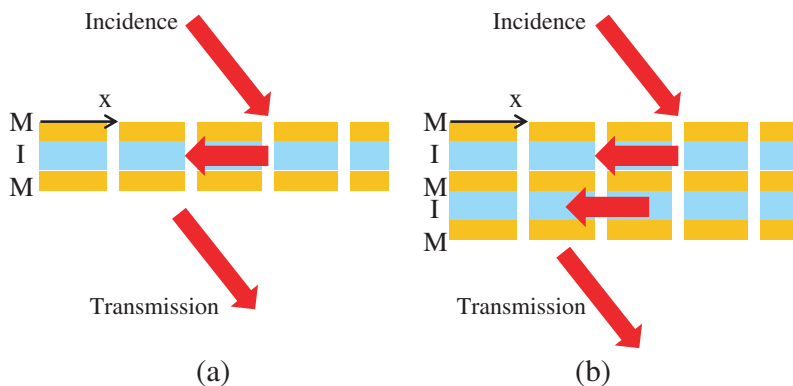
Figure 7. Schematic drawings of mechanism of in-plane backward shift of rays in fishnet MM slabs including (a) one I layer and (b) two I layers. The shift seemingly looks as if negative refraction from the outside.

We here compare the enhancement effect regarding the EM power flows. As for the in-plane EM power flows $P_{||}$, the enhancement factors, defined by the ratio of $P_{||}/P_{\text{in}}$, take the values of 2 to 5 in the fishnet MM of one I layer; for example, $P_{||}/P_{\text{in}} = 6.0/1.45 = 4.1$ at the lowest TM mode (see Figure 3). The factor $P_{||}/P_{\text{in}}$ took a larger value in the fishnet MM of two I layers; in fact, $P_{||}/P_{\text{in}} = 8.3$ (see Figure 6) and about twofold increase was observed for the one-I-layer fishnet MM. This was partially because the absorption increases in the two-I-layers fishnet MM. But only absorption is not the reason for the increase in the power flow. Actually, the absorptions are about 30% and 20% in the two-I-layers and one-I-layer fishnet MMs, respectively. Thus, further resonant enhancement plays a positive role in the power-flow enhancement by increasing the number of stacking layers. This result suggests that the more stacked fishnet MM offers better performance in waveguide applications.

In contrast, the power flow is not significantly enhanced at the reduced SPP mode. This is probably because the reduced SPP mode does not efficiently form in-plane power flow in any direction; instead, it induces locally enhanced EM fields at the interface. This is one of the features of the reduced SPP mode.

4. DISCUSSION

Figure 7 schematically depicts the EM power flow at the lower branch of the lowest TM mode. Figures 3 and 6 clearly show that in-plane modes are excited and have net negative flow to the incident power flow. The lateral backward shift looks as if negative refraction of rays from the outside. One of the features in the in-plane power flow is that the flow is not reduced by increasing the number of stacked layers (see Figure 6), enabling to obtain more thick MMs exhibiting the seeming negative refraction. Note that the EM dynamics inside the fishnet MMs at oblique incidence has been revealed by the direct numerical solutions without any model or simplification. Since the seeming negative refraction of rays are realized in a general way, many applications, for example, switch back of ray in micro-dimensions, will be conceived based on the lowest TM mode in the fishnet MMs.

In terms of the wavenumber conservation, the incident in-plane wavenumber $k_{||}$ is unequal to net in-plane wavenumber in the I layer, $k_{||}^I$. The discrepancy is compensated by a lattice momentum $2\pi/a$. The negative flow expressed with the $k_{||}^I$ satisfies the condition of an umklapp process,

$$k_{||}^I = k_{||} - \frac{2\pi}{a}, \tag{2}$$

and $k_{||}^I < 0$. Eq. (2) represents the conservation of wavenumber at the interface. The dispersion (the dotted line) in Figure 2(b) evidences the umklapp process. The excitations through the umklapp process result in the in-plane backward shift of rays as depicted in Figure 7. It is worth noting that umklapp processes generally take place in periodic media [35].

5. CONCLUSIONS

We have precisely resolved Maxwell equations for the fishnet MM slabs in the configuration of optical experiment and revealed the EM eigen modes. By evaluating light absorption spectra, the resonant energies of the eigen modes were explicitly determined, making it possible to obtain the dispersion diagrams. The lower TM modes and the reduced SPP mode were characterized by the dispersions and H field distributions. It was shown that the lower TM modes are MIM-inner modes and that the reduced SPP mode is an interface TM mode. The symmetry of the lower TM modes was also identified from group theory; the first and third modes were found to have 2D $\mathcal{E}$ symmetry. Besides, the resonant enhancements on the eigen modes

were quantitatively discussed. These features in the fishnet MMs were directly obtained without relying on the effective (ε, μ) framework or any other model proposed to MMs. Thus, the present first-principle analysis offers definite and deeper insights for the fishnet MMs, and moreover is a general procedure valid to other MM slabs.

ACKNOWLEDGMENT

APPENDIX A. FULL DISPERSION EQUATION FOR HOMOGENOUS MIM WAVEGUIDE MODES

Here we derive the full dispersion equation describing inner eigen modes in a homogeneous MIM structure. To keep generality, we think of the configuration shown in Figure A1. Stacked MIM layers of finite thickness are located between semi-infinitely thick insulators of permittivities ε_1 and ε_3. The thickness of the M and I layers is set to be d_M and d_I, respectively. The coordinate axes are defined as shown
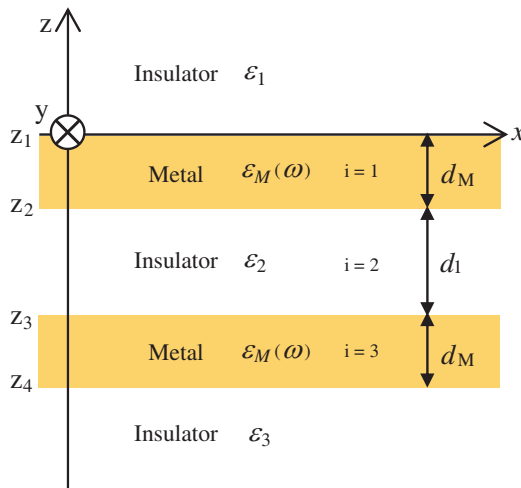

Figure 8. Configuration of a homogeneous MIM structure located between semi-infinitely thick insulators. The thickness of each layer and the permittivities are shown.

in Figure A1. The permittivity of metal is written as $\varepsilon_M(\omega)$ and that of insulator inside the MIM structure is ε_2.

The planar modes in the homogeneous MIM structure are exponentially decreasing solutions in the semi-infinitely thick insulator layers; the z dependence of E field is expressed as

$$E_\pm(z) = E_\pm \exp(\pm k_z^{(\pm)} z) \tag{A1}$$

and $\mathrm{Re}(k_z^{(\pm)}) < 0$ where $k_z^{(\pm)}$ is the z component of wavevector. The z dependence satisfies $E_\pm(z) \to 0$ as $z \to \pm\infty$, respectively. In the layers of finite thickness, the z dependence is written as

$$E_l(z) = E_l^+ \exp(ik_z^{(l)} z) + E_l^- \exp(-ik_z^{(l)} z) \tag{A2}$$

where $l = 1, 2, 3$. General expressions of Eqs. (A1) and (A2) are connected to each other at the boundaries of $z = z_j$ $(j = 1, 2, 3, 4)$. By eliminating the terms of $E_\pm$, E_l, $k_z^{(\pm)}$ and $k_z^{(l)}$, the dispersion equation for the planar modes is finally obtained:

$$\left\{ \exp\left(2\sqrt{k_0^2\varepsilon_1 - k_\parallel^2}\, d_I\right) - 1 \right\} \left(1 - \frac{k_0^2\varepsilon_1 - k_\parallel^2}{\varepsilon_1^2} \frac{\varepsilon_M^2(\omega)}{k_0^2\varepsilon_M(\omega) - k_\parallel^2} \right)$$

$$\times \left(1 + \frac{1 + \frac{\sqrt{k_0^2\varepsilon_M(\omega) - k_\parallel^2}}{\varepsilon_M(\omega)} \frac{\varepsilon_1}{\sqrt{k_0^2\varepsilon_1 - k_\parallel^2}}}{1 - \frac{\sqrt{k_0^2\varepsilon_M(\omega) - k_\parallel^2}}{\varepsilon_M(\omega)} \frac{\varepsilon_1}{\sqrt{k_0^2\varepsilon_1 - k_\parallel^2}}} \cdot \frac{\frac{\sqrt{k_0^2\varepsilon_M(\omega) - k_\parallel^2}}{\varepsilon_M(\omega)} \frac{\varepsilon_3}{\sqrt{k_0^2\varepsilon_3 - k_\parallel^2}} - 1}{\frac{\sqrt{k_0^2\varepsilon_M(\omega) - k_\parallel^2}}{\varepsilon_M(\omega)} \frac{\varepsilon_3}{\sqrt{k_0^2\varepsilon_3 - k_\parallel^2}} + 1} \right)$$

$$+ \left\{ \exp\left(2\sqrt{k_0^2\varepsilon_1 - k_\parallel^2}\, d_I\right) \left(1 + \frac{\sqrt{k_0^2\varepsilon_1 - k_\parallel^2}}{\varepsilon_1} \frac{\varepsilon_M(\omega)}{\sqrt{k_0^2\varepsilon_M(\omega) - k_\parallel^2}} \right)^2 \right.$$

$$\left. - \left(1 - \frac{\sqrt{k_0^2\varepsilon_1 - k_\parallel^2}}{\varepsilon_1} \frac{\varepsilon_M(\omega)}{\sqrt{k_0^2\varepsilon_M(\omega) - k_\parallel^2}} \right)^2 \right\}$$

$$\times \exp\left(-2\sqrt{k_0^2\varepsilon_M(\omega) - k_\parallel^2}\, d_M\right) \frac{\frac{\sqrt{k_0^2\varepsilon_M(\omega) - k_\parallel^2}}{\varepsilon_M(\omega)} \frac{\varepsilon_3}{\sqrt{k_0^2\varepsilon_3 - k_\parallel^2}} - 1}{\frac{\sqrt{k_0^2\varepsilon_M(\omega) - k_\parallel^2}}{\varepsilon_M(\omega)} \frac{\varepsilon_3}{\sqrt{k_0^2\varepsilon_3 - k_\parallel^2}} + 1}$$

$$+\left\{\exp\left(2\sqrt{k_0^2\varepsilon_1-k_\parallel^2}d_I\right)\left(1+\frac{\sqrt{k_0^2\varepsilon_1-k_\parallel^2}}{\varepsilon_1}\frac{\varepsilon_M(\omega)}{\sqrt{k_0^2\varepsilon_M(\omega)-k_\parallel^2}}\right)^2\right.$$

$$-\left.\left(1-\frac{\sqrt{k_0^2\varepsilon_1-k_\parallel^2}}{\varepsilon_1}\frac{\varepsilon_M(\omega)}{\sqrt{k_0^2\varepsilon_M(\omega)-k_\parallel^2}}\right)^2\right\}$$

$$\times\exp\left(2\sqrt{k_0^2\varepsilon_M(\omega)-k_\parallel^2}d_M\right)\frac{1+\frac{\sqrt{k_0^2\varepsilon_M(\omega)-k_\parallel^2}}{\varepsilon_M(\omega)}\frac{\varepsilon_1}{\sqrt{k_0^2\varepsilon_1-k_\parallel^2}}}{1-\frac{\sqrt{k_0^2\varepsilon_M(\omega)-k_\parallel^2}}{\varepsilon_M(\omega)}\frac{\varepsilon_1}{\sqrt{k_0^2\varepsilon_1-k_\parallel^2}}}=0.\text{(A3)}$$

For simplicity, the notation of k_0 is used, defined by $k_0 = \omega/c$ where ω is angular frequency of the EM wave. Eq. (A3) provides the relation of $k_\parallel$ and ω. The solutions of Eq. (A3) are dispersion curves of planar waveguide modes in the homogeneous MIM structure.

In the present analysis, the semi-infinitely thick layers are air, the metal is Au, and the insulator layer of finite thickness is composed of Al$_2$O$_3$. Accordingly, the permittivities of insulators were set to be $\varepsilon_1 = \varepsilon_3 = 1.00054$ and $\varepsilon_2 = 2.7225$. The permittivity of Au, $\varepsilon_M(\omega)$, was taken from the literature [30]. Although Eq. (A3) has several solutions, only the lowest one in energy contributes to describing the modes in Figure 2(b). The lowest solution in Eq. (A3) was numerically found, which is shown in Figure 2(b) by the dashed line. The higher modes are very close to the light cone in Figure 2(a) and therefore are not shown.

REFERENCES

1. Itoh, T. and C. Caloz, *Electromagnetic Metamaterials*, Wiley, New York, 2005.

2. Pendry, J. B. and D. R. Smith, "Reversing light with negative refraction," *Phys. Today*, Vol. 57, No. 6, 37–41, 2004.

3. Solymar, L. and E. Shamonina, *Waves in Metamaterials*, Oxford University Press, Oxford, 2009.

4. Soukoulis, C. M. and M. Wegener, "Past achievements and future challenges in the development of three-dimensional photonic metamaterials," *Nature Photon.*, Vol. 5, No. 9, 523–530, 2011.

5. Fang, N., D. Xi, J. Xu, M. Ambati, W. Srituravanich, C. Sun, and X. Zhang, "Ultrasonicmetamaterials with negative modulus," *Nature Mater.*, Vol. 5, No. 6, 452–456, 2006.

6. Zhang, S., L. Yin, and N. Fang, "Focusing ultrasound with an acoustic metamaterial network," *Phys. Rev. Lett.*, Vol. 102, No. 19, 194301, 2009.

7. Zhang, S., C. Xia, and N. Fang, "Broadband acoustic cloak for ultrasound waves," *Phys. Rev. Lett.*, Vol. 102, No. 2, 024301, 2011.

8. Smith, D. R., S. Schultz, P. Markoš, and C. M. Soukoulis, "Determination of effective permittivity and permeability of metamaterials from reflection and transmission coefficients," *Phys. Rev. B*, Vol. 65, No. 19, 195104, 2002.

9. Cho, K., *Reconstruction of Macroscopic Maxwell Equations*, Springer, Berlin, 2010.

10. Iwanaga, M., "Subwavelength electromagnetic dynamics in stacked complementary plasmonic crystal slabs," *Opt. Express*, Vol. 18, No. 15, 15389–15398, 2010.

11. Iwanaga, M., "Electromagnetic eigenmodes in a stacked complementary plasmonic crystal slab," *Phys. Rev. B*, Vol. 82, No. 15, 155402, 2010.

12. Iwanaga, M., N. Ikeda, and Y. Sugimoto, "Enhancement of local electromagnetic fields in plasmonic crystals of coaxial metallic nanostructures," *Phys. Rev. B*, Vol. 85, No. 4, 045427, 2012.

13. Zhang, S., W. Fan, N. C. Panoiu, K. J. Malloy, R. M. Osgood, and S. R. J. Brueck, "Experimental demonstration of near-infrared negative-index metamaterials," *Phys. Rev. Lett.*, Vol. 95, No. 13, 137404, 2005.

14. Dolling, G., C. Enrich, M. Wegener, C. M. Soukoulis, and S. Linden, "Low-loss negative-index metamaterial at telecommunication wavelengths," *Opt. Lett.*, Vol. 31, No. 12, 1800–1802, 2006.

15. Dolling, G., M. Wegener, C. M. Soukoulis, and S. Linden, "Negative-index metamaterial at 780 nm wavelength," *Opt. Lett.*, Vol. 32, No. 1, 53–55, 2007.

16. Dolling, G., M. Wegener, and S. Linden, "Realization of a three-functional-layer negative-index photonic metamaterial," *Opt. Lett.*, Vol. 32, No. 5, 551–553, 2007.

17. Chettiar, U. K., A. V. Kildishev, H.-K. Yuan, W. Cai, S. Xiao, V. P. Drachev, and V. M. Shalaev, "Dual-band negative index metamaterial: Double negative at 813 nm and single negative at 772 nm," *Opt. Lett.*, Vol. 32, No. 12, 1671–1673, 2007.

18. Liu, N., L. Fu, S. Kaiser, H. Schweizer, and H. Giessen, "Plasmonic building blocks for magnetic molecules in three-dimensional optical metamaterials," *Adv. Mater.*, Vol. 20, No. 20,

3859–3865, 2008.

19. Valentine, J., S. Zhang, T. Zentgraf, E. Ulin-Avila, D. A. Genov, G. Bartal, and X. Zhang, "Three-dimensional optical metamaterial with a negative refractive index," *Nature*, Vol. 455, No. 7211, 376–379, 2008.

20. Xiao, S., U. K. Chettiar, A. V. Kildishev, V. P. Drachev, and V. M. Shalaev, "Yellow-light negative-index metamaterials," *Opt. Lett.*, Vol. 34, No. 22, 3478–3450, 2009.

21. Xiao, S., V. P. Drachev, A. V. Kildishev, X. Ni, U. K. Chettiar, H.-K. Yuan, and V. M. Shalaev, "Loss-free and active optical negative-index metamaterials," *Nature*, Vol. 466, No. 7307, 735–738, 2010.

22. Mary, A., S. G. Rodrigo, F. J. Garcia-Vidal, and L. Martin-Moreno, "Theory of negative-refractive-index response of double-fishnet structures," *Phys. Rev. Lett.*, Vol. 101, No. 10, 103902, 2008.

23. Parsons, J., E. Hendry, J. R. Sambles, and W. L. Barnes, "Localized surface-plasmon resonances and negative refractive index in nanostructured electromagnetic metamaterials," *Phys. Rev. B*, Vol. 80, No. 24, 245117, 2009.

24. García-Meca, C., J. Hurtado, J. Martí, A. Martínez, W. Dickson, and A. V. Zayats, "Low-loss multilayered metamaterial exhibiting a negative index of refraction at visible wavelengths," *Phys. Rev. Lett.*, Vol. 106, No. 6, 067402, 2011.

25. Yang, J., C. Sauvan, H. T. Liu, and P. Lalanne, "Theory of fishnet negative-index optical metamaterials," *Phys. Rev. Lett.*, Vol. 107, No. 4, 043903, 2011.

26. Cao, T. and M. J. Cryan, "Modeling of optical trapping using double negative index fishnet metamaterials," *Progress In Electromagnetics Research*, Vol. 129, 33–49, 2012.

27. Iwanaga, M., "In-plane plasmonic modes of negative group velocity in perforated waveguides," *Opt. Lett.*, Vol. 36, No. 13, 2504–2506, 2011.

28. Li, L., "New formulation of the fourier modal method for crossed surface-relief gratings," *J. Opt. Soc. Am. A*, Vol. 14, No. 10, 2758–2767, 1997.

29. Li, L., "Formulation and comparison of two recursive matrix algorithm for modeling layered diffraction gratings," *J. Opt. Soc. Am. A*, Vol. 13, No. 5, 1024–1035, 1996.

30. Rakić, A. D., A. B. Djurušić, J. M. Elazar, and M. L. Majewski, "Optical properties of metallic films for vertical-cavity optoelec-

tronic devices," *Appl. Opt.*, Vol. 37, No. 22, 5271–5283, 1998.

31. Fan, S. and J. D. Joannopoulos, "Analysis of guided resonances in photonic crystal slabs," *Phys. Rev. B*, Vol. 65, No. 23, 235112, 2002.

32. Swihart, J. C., "Field solution for a thin-film superconducting strip transmission line," *J. Appl. Phys.*, Vol. 32, No. 3, 461–469, 1961.

33. Economou, E. N., "Surface plasmons in thin films," *Phys. Rev.*, Vol. 182, No. 2, 539–554, 1969.

34. Sakoda, K., *Optical Properties of Photonic Crystals*, 2nd Edition, Springer, Berlin, 2005.

35. Ashcroft, N. W. and N. D. Mermin, *Solid State Physics*, Sauders College, Fort Worth, 1976.